ORIGINAL ARTICLE

Seepage-related characteristics of weak interlayer suffering from a physically-chemically mediated erosion in grotto relics

Junxia Wang[1]

Abstract

The coexistence of the weak interlayer and groundwater could give rise to an undesirable geological condition, resulting in seepage-induced hazards, particularly in grotto relics. Seepage-related characteristics of a weak interlayer affected by physically-chemically mediated erosion in grotto relics were investigated. As confirmed by the morphological features, nano-indentation experiments and Raman spectroscopy analysis, the weak interlayer exhibited characteristics of disintegrability in water and low mechanical strength. The average total content of clay minerals significantly increased from 25.2 to 28.5%, compared to the pre-experimental X-ray diffraction data, despite its non-uniformity, indicating a trend toward argillization. Based on mineralogical composition, hydro-chemical data and three-dimensional morphology before and after the experiment, the changes induced by physically-chemically mediated erosion were highlighted. A coherent explanation of the permeability evolution is that the physically-chemically mediated erosion leads to the formation of fracture channel in weak interlayer under long-term water erosion and hydraulic scouring. The permeability enhanced from of 10^{-7}–10^{-8} cm/s at the initial stage to 8.01–10^{-4} cm/s at the existence of fracture channel.

Keywords Permeability evolution · Weak interlayer · Physical–chemical erosion · Grotto relics

Introduction

A weak interlayer refers to a special and widely distributed weak structure plane in a rock mass, which is characteristics of low modulus, low strength, large deformation and a certain thickness sandwiched between hard rock layers (Dong et al. 2020; Gu and Huang 2016; Nan et al. 2021; Shang et al. 2018). It exerts a significant influence on the geological hazards in slopes, tunnels, highways, railways and so on (Gao et al. 2022; Hu et al. 2019; Li et al. 2021; Wei et al. 2022). Therefore, enough attention has been paid to the stability-related problem. In addition to the weak interlayer, groundwater is another unfavorable geological factor. It is prone to argillization when encountering water, leading to internal instability and crack propagation in the rock mass (Chen et al. 2021; Jin et al. 2018; Luo et al. 2022). Researches on the influence of the coexistence of seepage

and weak interlayers have primarily focused on stability-related problems. Nevertheless, few studies have examined the seepage-related disaster induced by weak interlayer. A weak interlayer with high plasticity and low strength may result in concentrated leakage pathways, and ultimately leading to seepage failure under the long-term influence of groundwater (Ye et al. 2011). Zhu et al. (2019) and Zhu et al. (2020a, b) focused on the scouring effect of water flow on a weak interlayer containing continuous cracks that were subjected to hydraulic scouring. They established an infinitely extended hydraulic scouring model based on the Navier–Stokes equation and the Brinkman–extended Darcy equation. The critical depth of soil particles when washed by water flow was determined by combining the flow velocity characteristics of water flow in the fracture with the force characteristics of the soil particles. Factually, except for hydraulic scouring, chemical erosion, particularly mineral dissolution in the subsurface, has led to significant alterations in porosity and permeability (Detwiler 2008). In fractured rock, individual fractures often act as the dominant seepage pathways and effective storage spaces for subsurface fluid flow and transport (Detwiler 2008; Zhu et al. 2020a, b). Water–rock interaction within variable apertures commonly

✉ Junxia Wang
jxwang@whrsm.ac.cn

1 State Key Laboratory of Geomechanics and Geotechnical Engineering, Institute of Rock and Soil Mechanics, Chinese Academy of Sciences, Wuhan 430071, China

contributes to the dissolution of minerals along fracture surfaces and alteration in fracture apertures, potentially altering the fracture permeability over time (Blaisonneau et al. 2016; Detwiler and Rajaram 2007). The dissolution rates are typically controlled by the kinetics of chemical reactions occurring at the water–rock interfaces, as well as the convective and diffusive transport of reactants and products within the fracture (Detwiler and Rajaram 2007).

Several studies have addressed the effect of dissolution on permeability. Detwiler and Rajaram (2007) presented a depth-averaged model for quantifying localized dissolution-induced alterations in fracture apertures. The model considers a smooth transition from reaction-limited dissolution to transport-limited dissolution. Kalia and Balakotaiah (2009) aimed to study the influence of medium heterogeneities on reactive dissolution of carbonates. They described the coupling between the transport and reaction process occurring at the pore and Darcy scales. The structure of the patterns formed during reactive dissolution and the amount of acid required to achieve a given increase in permeability are affected by the heterogeneity. Yasuhara et al. (2006) reported a flow-through experimental setup to elucidate the permeability evolution that resulted from stress-dependent and temperature-dependent dissolution. They underscored the significance of dissolution in determining the magnitude and the rates of permeability enhancement within fractured rock caused by chemical permeants in geothermal and petroleum reservoirs, where a lesser degree is pushed far from equilibrium under natural conditions. McGuire et al. (2013) explored the influences of stress, reactive chemistry and fracture roughness on the evolution of permeability in fractures. They combined a repeatable and constrained set of experiments and simulations to precisely identify a transition from pressurized solution to stress corrosion cracking-enhanced diffusion. The mechanically and chemically controlled changes in permeability evolution in fractured limestone were distinguished by applying the ratio of free-face dissolution to stress-corrosion-enhanced dissolution as an index. Polak et al. (2003) investigated the changes

in transport characteristics under thermal, stress, chemical environment based on flow-through experiment. It was found that the reduction of fracture permeability was monotonically related to the increase in temperature under constant effective stress, leading to the closure of the fracture. In comparison with the fracture closure and precipitation mechanism, it was suggested that dissolution at asperity contacts dominated the reduction of hydraulic aperture, as verified by the net removal of quartz. Shi et al. (2021) conducted tri-axial and long-term dissolution experiments to explore the temporal permeability and damage evolution of low-permeability sandstone caused by chemical reactions in conjunction with hydraulic fracturing. It was concluded that the increase in permeability resulted from both macroscopic fracture propagation and microscopic dissolution. However, the permeability evolution associated with the dissolution of weak interlayer by acidic or alkalescence solution was insufficient for evaluating the microstructure and dissolution characteristics.

Grottoes are widely distributed in China. Cracks development and cave collapse are accelerated under water seepage and water erosion (Su et al. 2023; Zhu et al. 2020a, b). Water seepage is a significant issue that not only threatens the appearance of grottoes but also becomes one of the main factors leading to the damage of grottoes and the most challenging work in grotto conservation (Lu et al. 2020; Sun et al. 2023; Wang 2023). As a representative of sandstone cultural grotto relics in China, Dazu Rock Carvings located in Chongqing were listed as a World Cultural Heritage site in 1999. Seepage-related disaster caused by weak interlayer has been observed in Dazu Rock Carvings, as illustrated in Fig. 1. An in-depth understanding of the physical–chemical phenomena occurring within the weak interlayer is essential. The evolution of permeability during a chemically mediated process is crucial for addressing the water seepage disaster in grotto relics. This article was designed with to characterize the physical–chemical phenomena that occurred on the weak interlayer during chemical corrosion and their roles in the evolution of permeability, in which the convection and

Fig. 1 The typical seepage-related disaster caused by weak interlayer in No. 168 cave in Dazu Beishan Rock Carvings
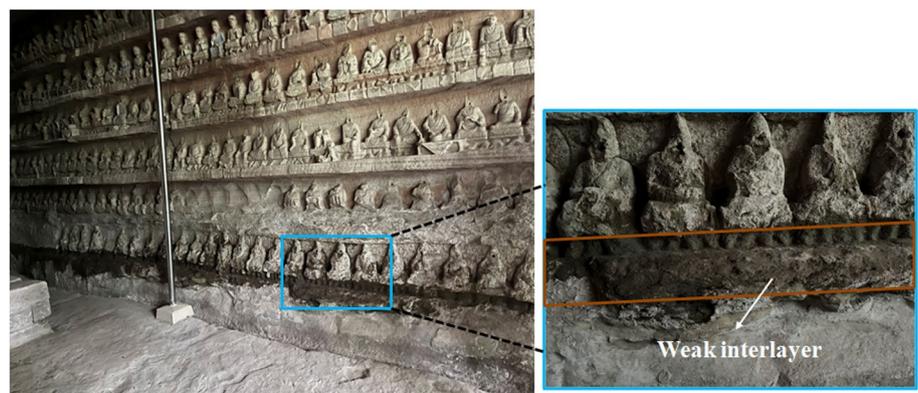
diffusion phenomena described by some authors are limited in this context.

Experimental details

The weak interlayer sample ($300 \times 100 \times 50$ mm) was gathered from Dazu Rock Carvings in Chongqing. The upper part was weak interlayer and the lower part was intact sandstone. In order to explore the physical–chemical phenomena that occurred within weak interlayer, six samples (Z1–Z6, $30 \times 30 \times 20$ mm) were prepared by means of wire-electrode cutting, as shown in Fig. 2. Samples of Z1 and Z4 were immersed into faintly acidic groundwater with pH = 6–7, involving comparative immersions of alkalescence groundwater with pH = 7–8 for samples of Z2 and Z5, and deionized water with pH = 7–8 for samples of Z3 and Z6.

Part of the residual samples was processed into a flat sample ($10 \times 10 \times 10$ mm) for mechanical measurement and the others were crushed to less than 2 mm in diameter for mineralogical measurement. The mineralogical and micro-structural observation were conducted using X-ray diffraction (XRD, D8 Advance) and scanning electron microscope (SEM, Quanta250). The porosity and pore size distribution of the samples were obtained by aperture distribution measuring instrument (NOVA1000e) based on gas absorption method. The nano-indentation hardness and modulus of the weak interlayer were measured by a high prescision nonmechanics tester (APEX),

in which the elastic modulus and poisson ratio of the applied indenter was 1140 GPa and 0.07, respectively. The three-dimensional geometry of the roughened surface was scanned using a composite laser knife scanner (Artec Spider). The digitized data were exported in *xyz* file format to evaluate pre-experimental and post-experimental variations related to physical–chemical reactivity (Huang et al. 2017; Tse 1979; Zhou et al. 2020). Changes in hydro-chemical composition of the immersion solution were analyzed by inductively coupled plasma atomic emission spectrometry (ICP-OES) and ion chromatography spectrometry (ICS), taking major cations (K^+, Na^+, Ca^{2+}, Mg^{2+}) and anions (HCO_3^-, Cl^-, NO_3^-, SO_4^{2-}) into consideration.

Results and discussion

Morphological features

Through visual description using an optical microscope, a micro-crack can be observed in the dry state of the upper weak interlayer before water immersion, as shown in Fig. 3. After water immersion, disintegration occurred, and micro-crack expanded along a pre-existing micro fracture, owing to high free swelling ratio($\sim 60\%$) of weak interlayer (Jian et al. 2005; Zhang et al. 2023) and stress relief to free boundaries contribute to the evolution of the overall permeability. By
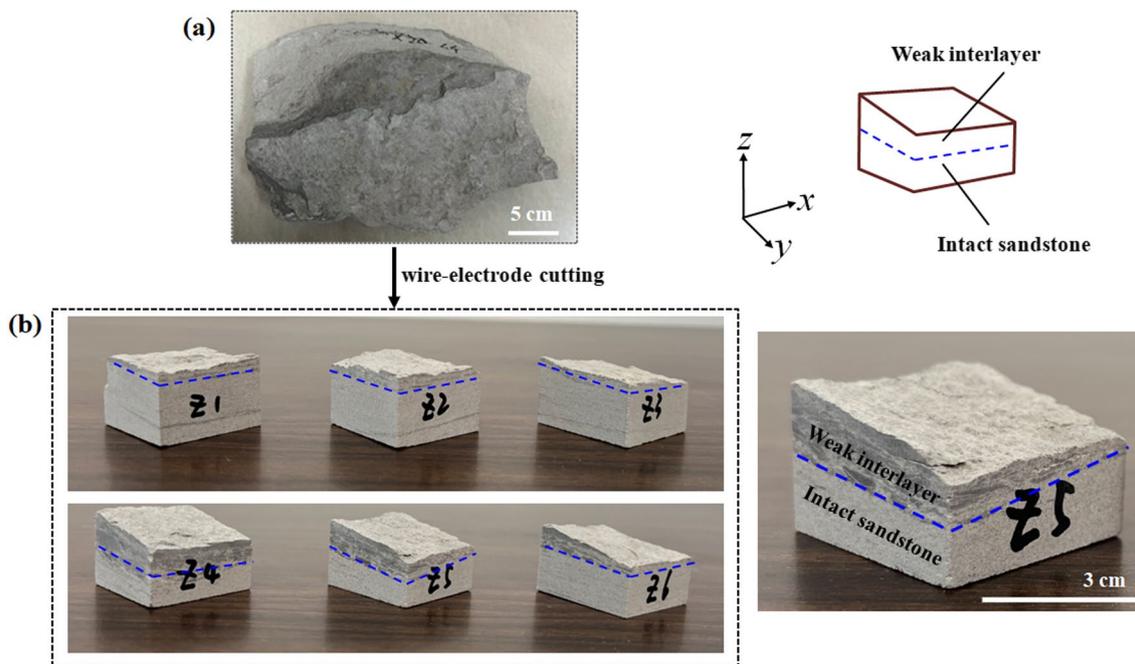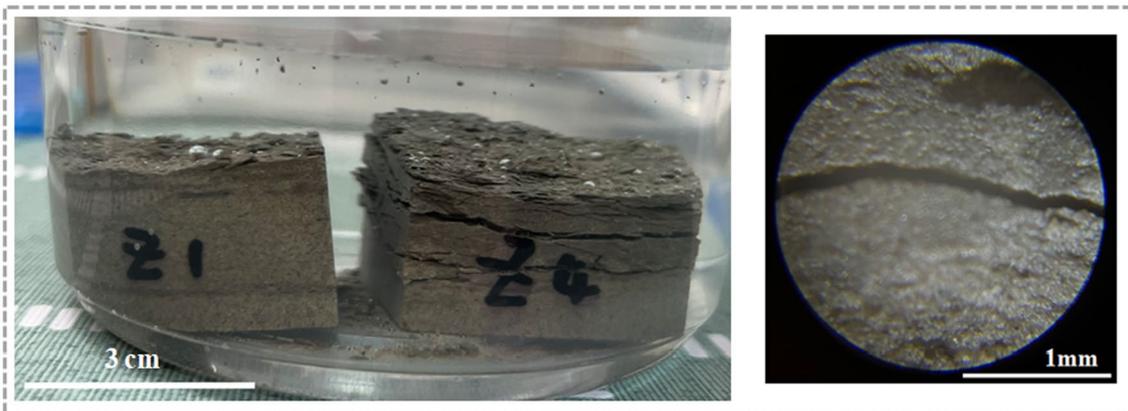

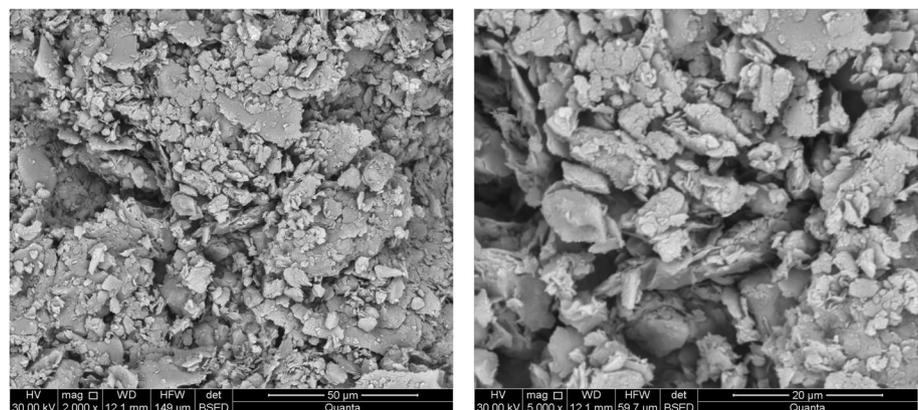**Fig. 2** **a** Sample collection and **b** preparation of weak interlayer

(a) Before water immersion

(b) After water immersion

Fig. 3 The micro-images comparison of weak interlayer **a** before and **b** after water immersion

Fig. 4 The SEM micrograph of weak interlayer: **a** ×2000; **b** ×5000

（a）2000×   （b）5000×

adding supplementary observations using SEM in Fig. 4, loose structure became apparent, revealing a significant number of micro-voids and flake-like/granular-like clay minerals.

Nano-mechanical strength

The mechanical properties of rocks are related to mineral composition, particle type, particle size and other factors. In order to deterimine the nano-mechanical strength of filled medium, a nano-indentation test was conducted. Two

different areas were selected on the surface of weak interlayer(1 cm × 1 cm × 1 cm). Each micro-region consists of 9 measuring points distributed in the form of lattice and the interval of each group of measuring points is 60 μm, as illustrated in Fig. 5. The entire loading-hold-unloading process takes 30 s. Figure 6 presents the load–displacement curves at different measuring points in two indentation lattice micro-region. The variation trend is roughly similar and there is certain discreteness among the curves, mainly caused by the heterogeneity of weak interlayer. During the loading stage, the depth of the indenter into the weak interlayer increases rapidly. During the load-holding stage, the surface of weak interlayer experiences additional creep deformation. During the unloading stage, the elastic deformation of the weak interlayer quickly recovers, while the plastic deformation of a small portion remains unrecoverable.

Nano-indentation hardness (H) is the measurement of load bearing capacity of materials per unit area and its expression is listed as follows:

$$H = P_{\max}/A, \tag{1}$$

where P_{max} is the maximum load exerted on the indenter and A is the projected area of the contact surface between the head and the sample under loading.

According to the slope of the unloading curve, the contact stiffness S of the weak interlayer can be obtained according to reduced elastic modulus (E_r):

$$S = \frac{dP}{dh} = \frac{2}{\sqrt{\pi}} E_r \sqrt{A} \tag{2}$$

E_r can be derived according the following formula (Oliver and Pharr 1992, 2004):

$$\frac{1}{E_r} = \left(\frac{1 - \nu_s^2}{E_s}\right) + \left(\frac{1 - \nu_i^2}{E_i}\right) \tag{3}$$

where E_i and ν_i are the elastic modulus and poisson ratio of the indenter, respectively. E_s and ν_s are the elastic modulus and poisson ratio of the weak interlayer.
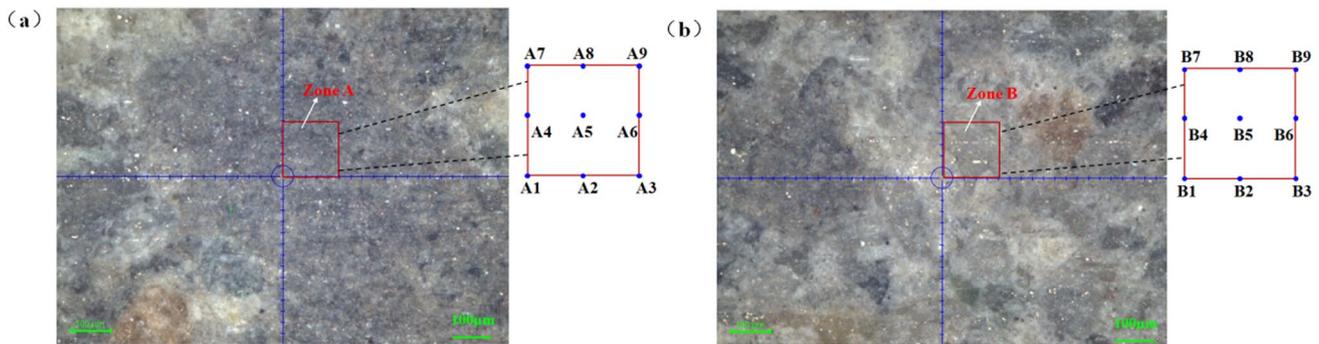

Fig. 5 The micro-region morphology of weak interlayer in nano-indentation test for illustrating **a** Zone A and **b** Zone B
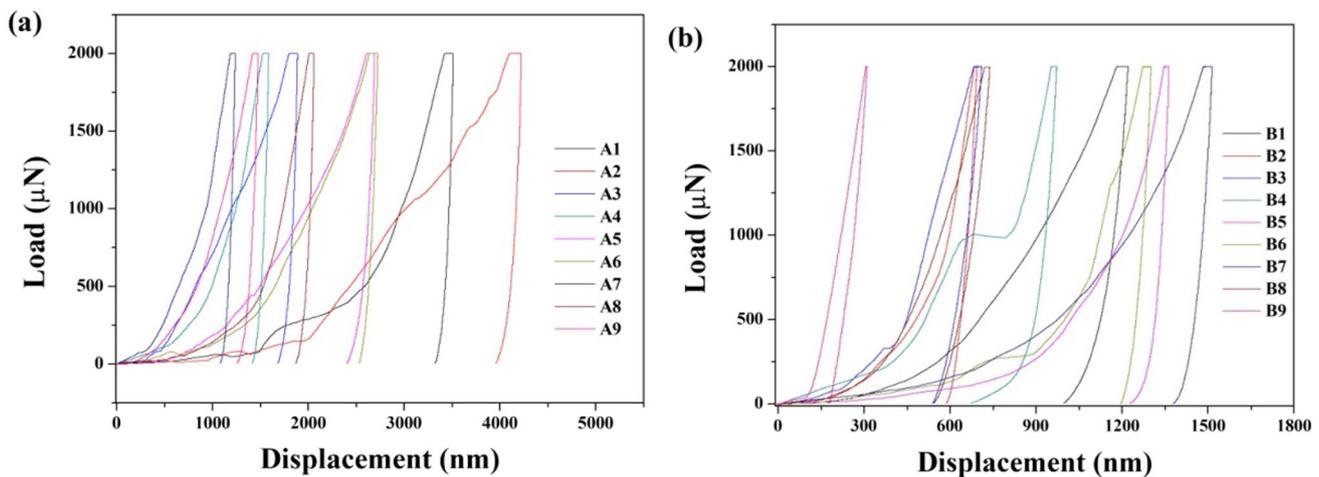

Fig. 6 The load–displacement curves at different measuring points in two indentation lattice micro-region of **a** Zone A and **b** Zone B

On basis of the nano-indentation load–displacement and the formula provided above, the nano-mechanical parameters for each measuring point can be calculated, as shown in Table 1. The elastic modulus is mainly concentrated in 1–5GPa in zone A and it is broadly distributed in the range of 3–15GPa in zone B, the indentation hardness of zone A is distributed among 10–50 MPa. While in zone B, it varies widely from 30 to 160 MPa. The nano-mechanical properties of different indentation point present some differences, which are closely attributed to the mineral types.

Raman spectroscopy analysis

The Raman spectra of minerals that yield identifiable peaks were displayed in Fig. 7. Figure 7a depicted the fingerprint peaks at 1086, 713, 281 and 156 cm^{-1} corresponding to the characteristic peaks of $CaCO_3$ crystallized in calcite structure, in comparison with RRUFF database (Korsakov et al. 2010; Murphy et al. 2021). The prominent peak at 1086 cm^{-1} can be assigned to the symmetric stretching mode of vibration (ν_1) of CO_3^{2-} group. The other weaker peaks at 713, 281 and 156 cm^{-1} were dominated by the symmetric bending, vibration and translation of CO_3^{2-} group, respectively (Garcia et al. 2007). The Raman spectra in Fig. 7b showed a triplet and strong peaks at 514, 734 and 452 cm^{-1}, a triplet and relatively weak peaks at 179, 148 and 129 cm^{-1}, two weak peaks at 287 and 264 cm^{-1}, the other two weaker peaks at 814 and 748 cm^{-1}. These peaks can be correlated with the presence of feldspar. There was a slight Raman

shift for clay minerals, making it difficult to obtain identifiable Raman spectra (Prinsloo et al. 2013). This challenge may be attributed to the pre-resonance condition and the weak laser response in the range of 0–3400 cm^{-1}, as shown in Fig. 7c. Anatase (TiO_2) was detected with a sharp peaks at 144, as illustrated in Fig. 7d. The distribution mapping of major minerals can be obtained by Raman plane scanning of the micro-region in the nano-indentation test, as displayed in Fig. 8. The location of the micro-region in the Raman plane scanning was essentially consistent with that in the nano-indentation test. Combined with the results of the nano-indentation test, it was deduced that the indentation hardness of clay minerals was mainly concentrated in the range of 33–53 MPa, while that of feldspar was broadly distributed from 150 to 164 MPa. Calcite, on the other hand, had an approximate indentation hardness of 1000 MPa.

Mineralogical characterization

As closely observed in Fig. 9, the major difference between the upper weak interlayer and the lower intact sandstone before the experiment is the composition K-feldspar and clay mineral. For the weak interlayer, albite was the dominant feldspar mineral, and 25.2 wt% of the clay minerals (illite, kaolinite and montmorillonite) were the accessory minerals. Nevertheless, it is composed of 54.3 wt% K-feldspar and 8.2 wt% clay minerals in the lower intact sandstone.

The XRD patterns of weak interlayer after experiment were illustrated in Fig. 10 and their mineral compositions were calculated by means of semi-quantitative method. Even though the mineral distribution in the weak interlayer is not uniform, the mineral composition after experiment was compared with the data before experiment as listed in Table 2. It was worth mentioning that the contents of illite and kaolinite in the three samples increased, leading to a higher total content of clay minerals and indicating a trend toward argillization.

Porosity and pore size distribution

The pore sizes were broadly distributed and classified as micro-porosity (with pore diameter < 2 nm), meso-pore (with pore diameter of 2–50 nm), and macro-pore (with pore diameter > 50 nm) (Sing 1985). Meso-pores with a pore size greater than 2 nm are dominated by long-range interactions (the osmotic swelling regime), while micro-pores with a pore size less than 2 nm are controlled by short-range interactions (the crystalline swelling regime) (Bourg and Ajo-Franklin 2017). Figure 11a displayed the isothermal curve of the weak interlayer. When the relative pressure (P/P_0) was less than 0.5, the absorption isotherm increased gradually and plateaued. As P/P_0 was greater than 0.5, the absorption isotherm and absorption amount presented a

Table 1 The nano-mechanical parameters of each measuring points of the weak interlayer

| Points	P_{max} (μN)	S (μN /nm)	A (nm^2)	E_r (GPa)	H (MPa)
A1	1998.524	25.958	3.161E+08	1.294	6.323
A2	1998.361	19.410	4.519E+08	0.809	4.422
A3	1997.926	24.640	9.199E+07	2.276	21.719
A4	1998.012	27.484	6.523E+07	3.015	30.630
A5	1998.352	17.710	1.835E+08	1.158	10.891
A6	1998.482	23.530	1.900E+08	1.513	10.521
A7	1998.206	29.309	3.975E+07	4.119	50.270
A8	1998.434	26.971	1.099E+08	2.280	18.191
A9	1998.090	23.741	5.580E+07	2.816	35.810
B1	1998.367	22.571	3.800E+07	3.244	52.583
B2	1997.957	37.247	1.258E+07	9.306	158.872
B3	1998.136	21.711	1.220E+07	5.507	163.790
B4	1998.341	28.942	2.451E+07	5.180	81.547
B5	1998.359	44.449	4.973E+07	5.585	40.185
B6	1998.273	39.386	4.501E+07	5.202	44.399
B7	1998.404	34.244	6.041E+07	3.904	33.079
B8	1997.983	19.396	1.300E+07	4.767	153.718
B9	1998.491	25.151	1.952E+06	15.949	1023.710

Fig. 7 The Raman spectra of **a** Calcite, **b** Feldspar, **c** Clay minerals and **d** Anatase in weak interlayer
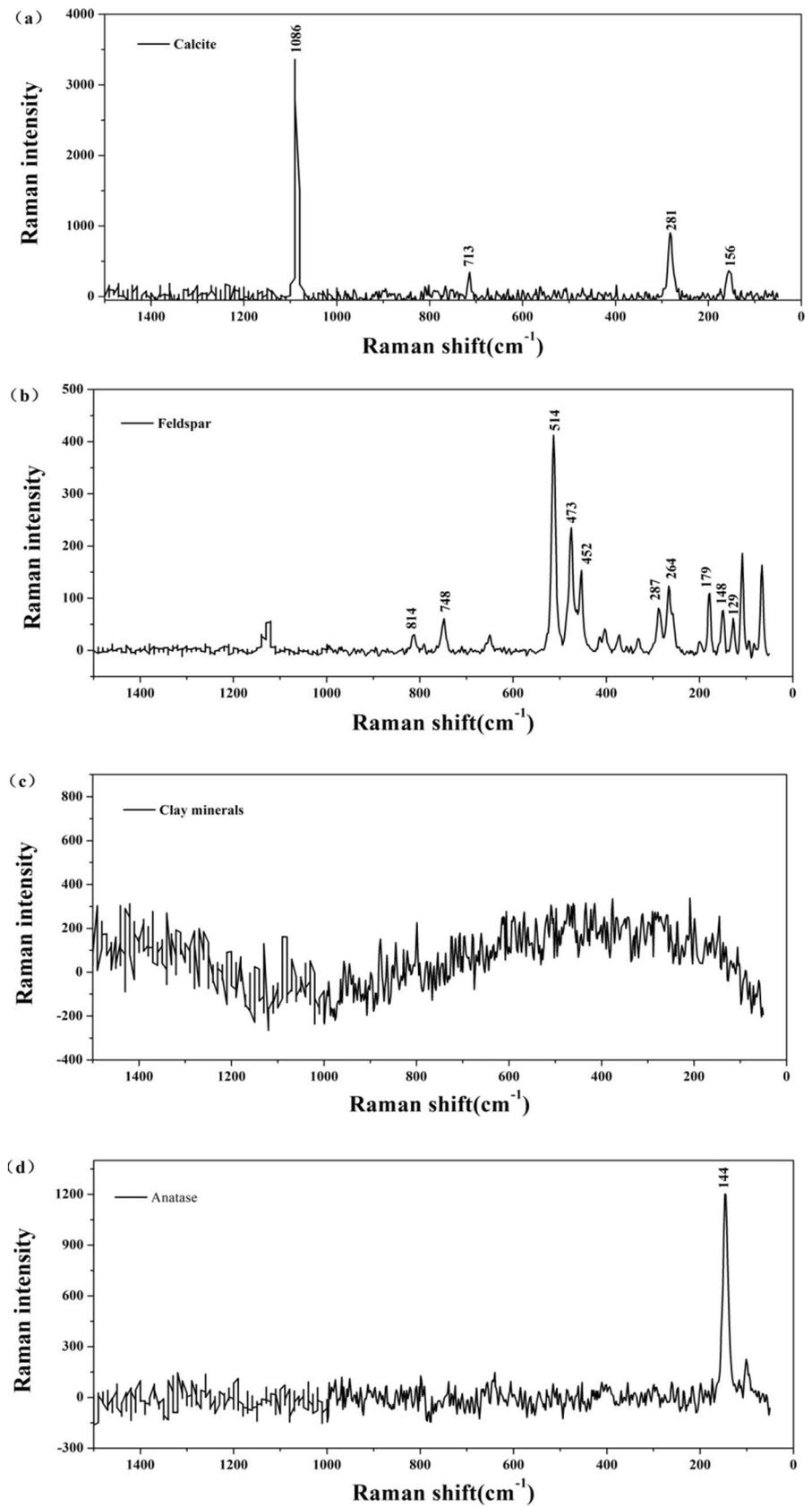
Fig. 8 **a** The location of the micro-region in the Raman plane scanning and **b** the distribution mapping of major minerals in Zone B. The green area, blue area and red area represented calcite, feldspar and clay minerals, respectively
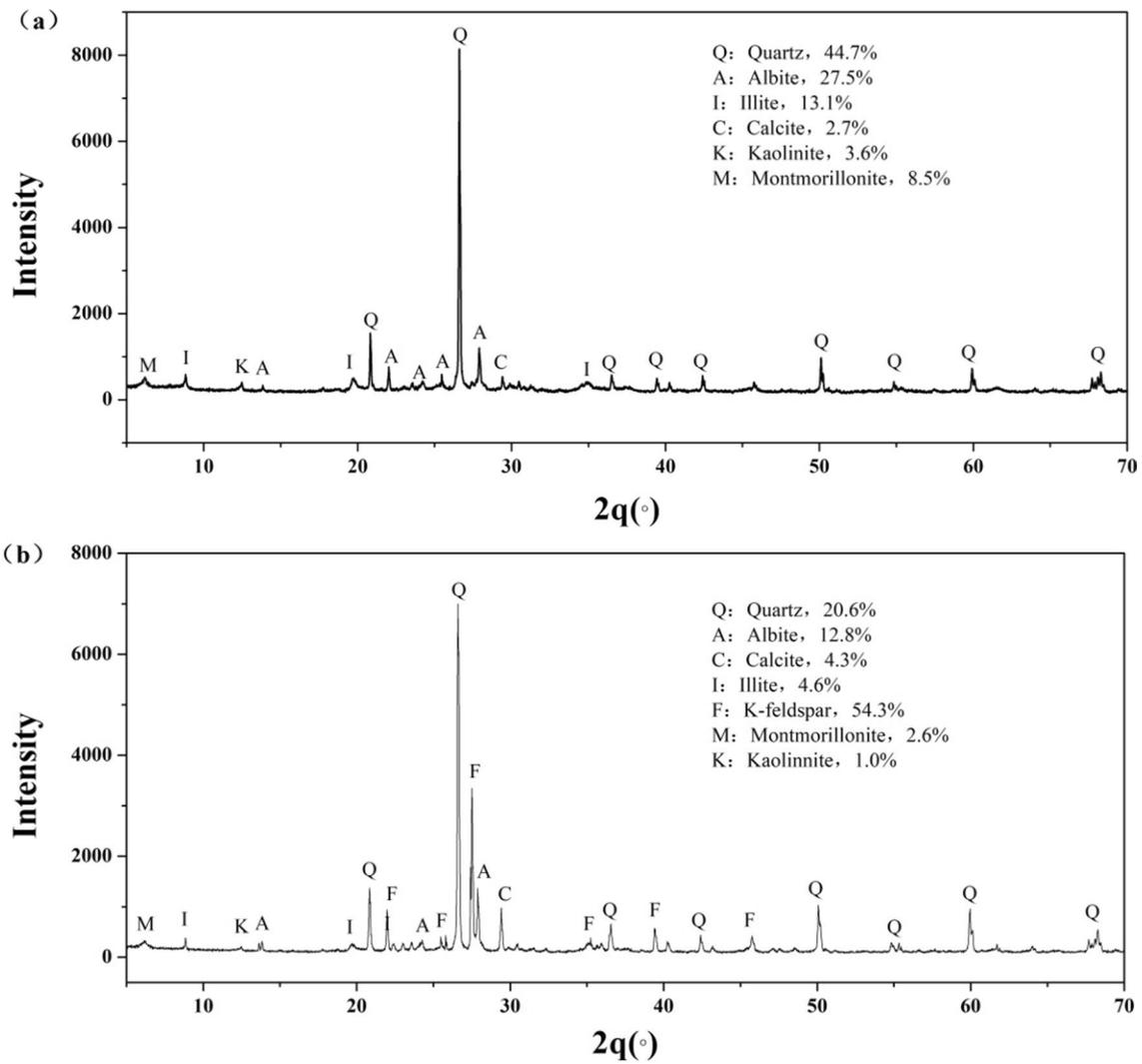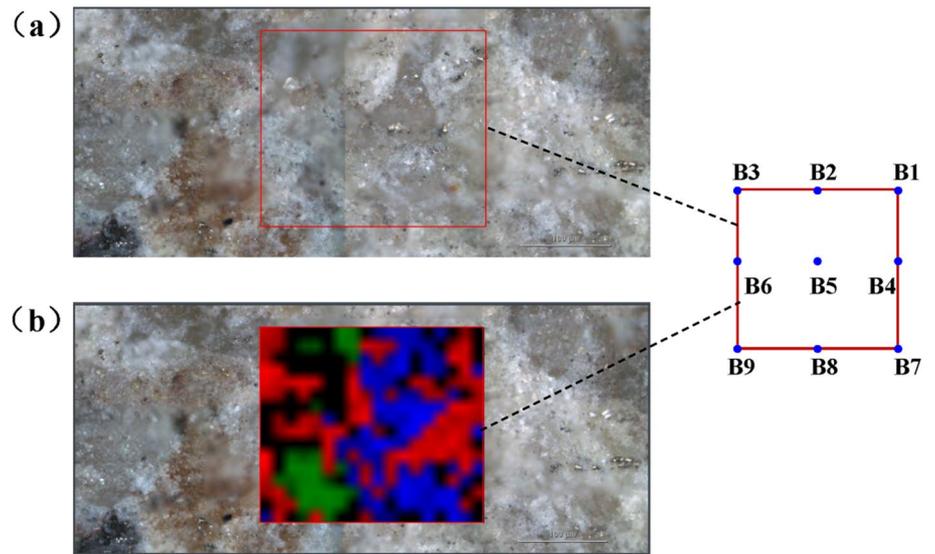
Fig. 9 The XRD patterns of **a** weak interlayer and **b** intact sandstone before experiment
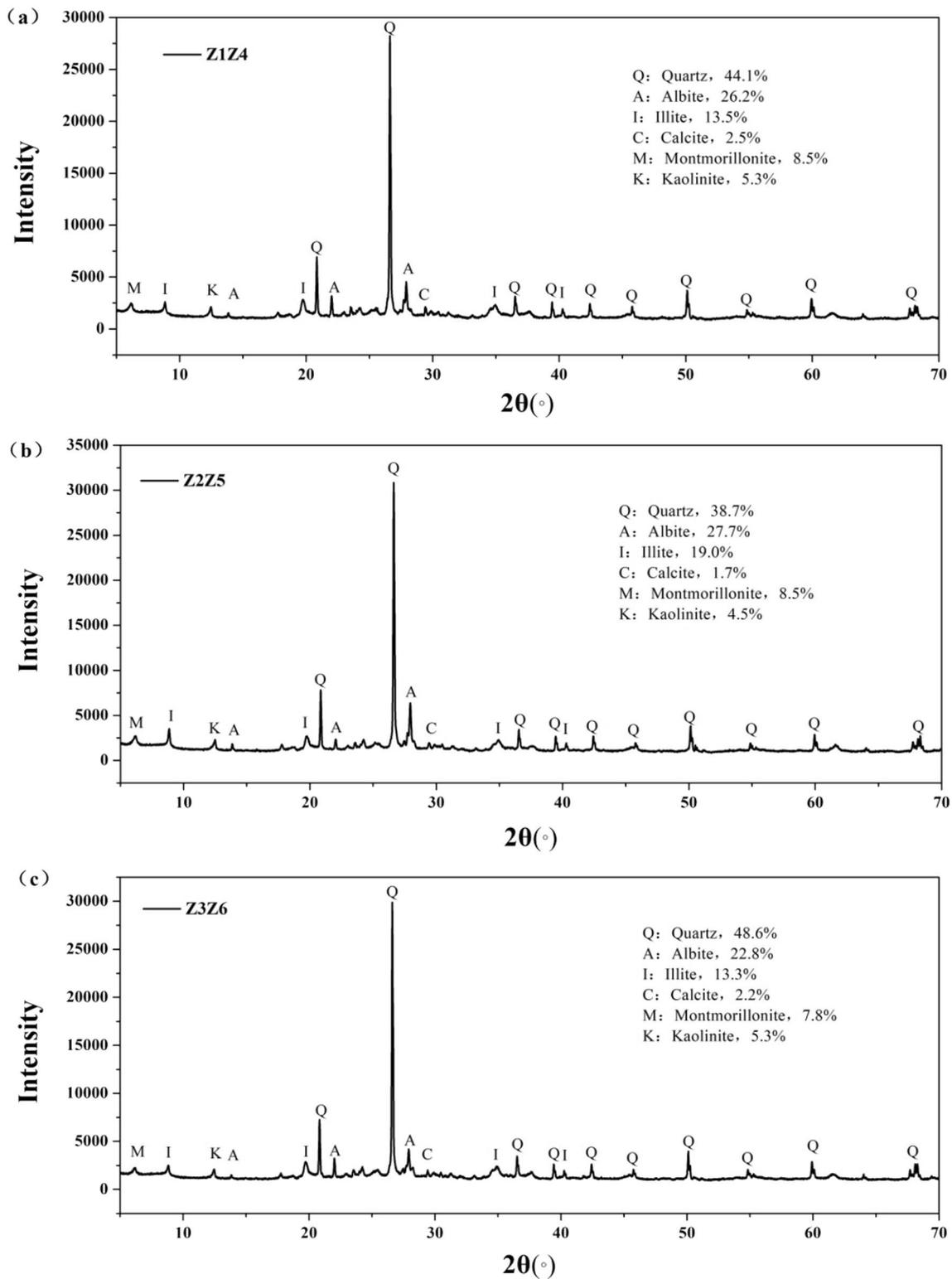
Fig. 10 The XRD patterns of weak interlayer for **a** Z1 and Z4, **b** Z2 and Z5 and **c** Z3 and Z6 after experiment

sharp rise, resulting in a typical IV-type isotherm, which was most likely associated with the meso-porous pores. The typical characteristics was that the absorption branch of the isotherm is inconsistent with the desorption branch, showing an obvious H3 hysteresis loop, where the slope of the curve continuously increased in the high-pressure region.

Table 2 Pre-experimental and post-experimental comparison of mineral composition of weak interlayer before and after experiment

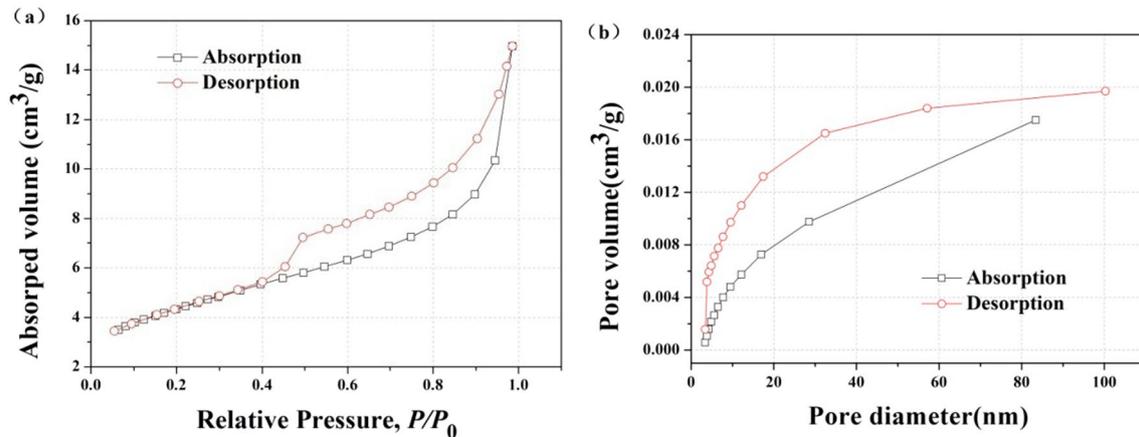|	Quartz	Albite	Illite	Calcite	Montmorillonite	Kaolinite	Clay minerals
Pre-experiment	44.7	27.5	13.1	2.7	8.5	3.6	25.2
Post-experiment							
Z1Z4	44.1	26.2	13.5	2.5	8.5	5.3	27.3
Z2Z5	38.7	27.7	19.0	1.7	8.5	4.5	31.9
Z3Z6	48.6	22.8	13.3	2.2	7.8	5.3	26.4
Average	43.8	25.6	15.3	2.1	8.3	5.0	28.5
Standard deviation	4.06	2.04	2.65	0.35	0.31	0.38	2.44

Fig. 11 a The isothermal curve of adsorption–desorption of weak interlayer and **b** the pore size distribution characteristic curve of weak interlayer. P is the equilibrium pressure of adsorbed gas and P_0 is the saturated vapor pressure of the adsorbed gas at the adsorption temperature

Figure 11b plotted the pore size distribution curve of the weak interlayer. The pore diameter mainly ranged from 3 to 20 nm and the total pore volume is 0.023cm³/g, with an average pore size of 6.16 nm and porosity of 7.11%.

Three-dimensional morphology

The roughness at sample scale is depicted by a height (z) map of the voids before and after experiment in Fig. 12, as derived from geo-statistical calculations. The physical characterizations (see Table 3) were carried out on the fracture asperities for highlighting the pre-experimental and post-experimental variations related to physical–chemical reactivity.

The average height (z_{avg}) can be calculated according to formula (4):

$$z_{avg} = \frac{1}{L} \int_0^L |z(x)| dx = \frac{1}{n} \sum_{i=1}^n |z_i|, \qquad (4)$$

where $z(x)$ is the contour height of each point, L is the length, n is the number of measuring points, z_i is the height of measuring point i。

Hydro-chemical variation

Table 4 listed the pre-experimental and post-experimental comparison of ionic concentration in immersion solution. As the weak interlayer (sample of Z2, Z5) was immersed by the ion-rich groundwater with pH = 7–8, the content of Na⁺ ions significantly increased and the content of Ca²⁺ and Mg²⁺ ions obviously decreased in comparison with the pre-experiment value. This indicated that the weak interlayer encountered ion exchange, absorption and dissolution reactions when exposed to an alkalescence solution. In this process, the soluble salt dissolved into the groundwater. The Na⁺ ions that were absorbed on the surface of the clay particles were gradually replaced by Ca²⁺ and Mg²⁺ ions in the groundwater. This replacement followed the order of cation exchange capacity ($Ca^{2+} > Mg^{2+} > K^+ > Na^+$) reported by Sun et al. (Sun et al. 2022). Montmorillonite were characteristics of high dispersion, large specific surface area, significant isomorphic substitution and a considerable amount of negative charge. Especially, its interlayer structure can absorb cations and the cation exchange capacity is 47.84–67.58 mg equivalent/100 g (Wang 1980). When the immersion solution was changed from alkalescence groundwater to deionized water, a significant increase in Na⁺ content and a slight increase

Fig. 12 The surface morphology diagrams of weak interlayer in comparison of pre-experiment and post-experiment
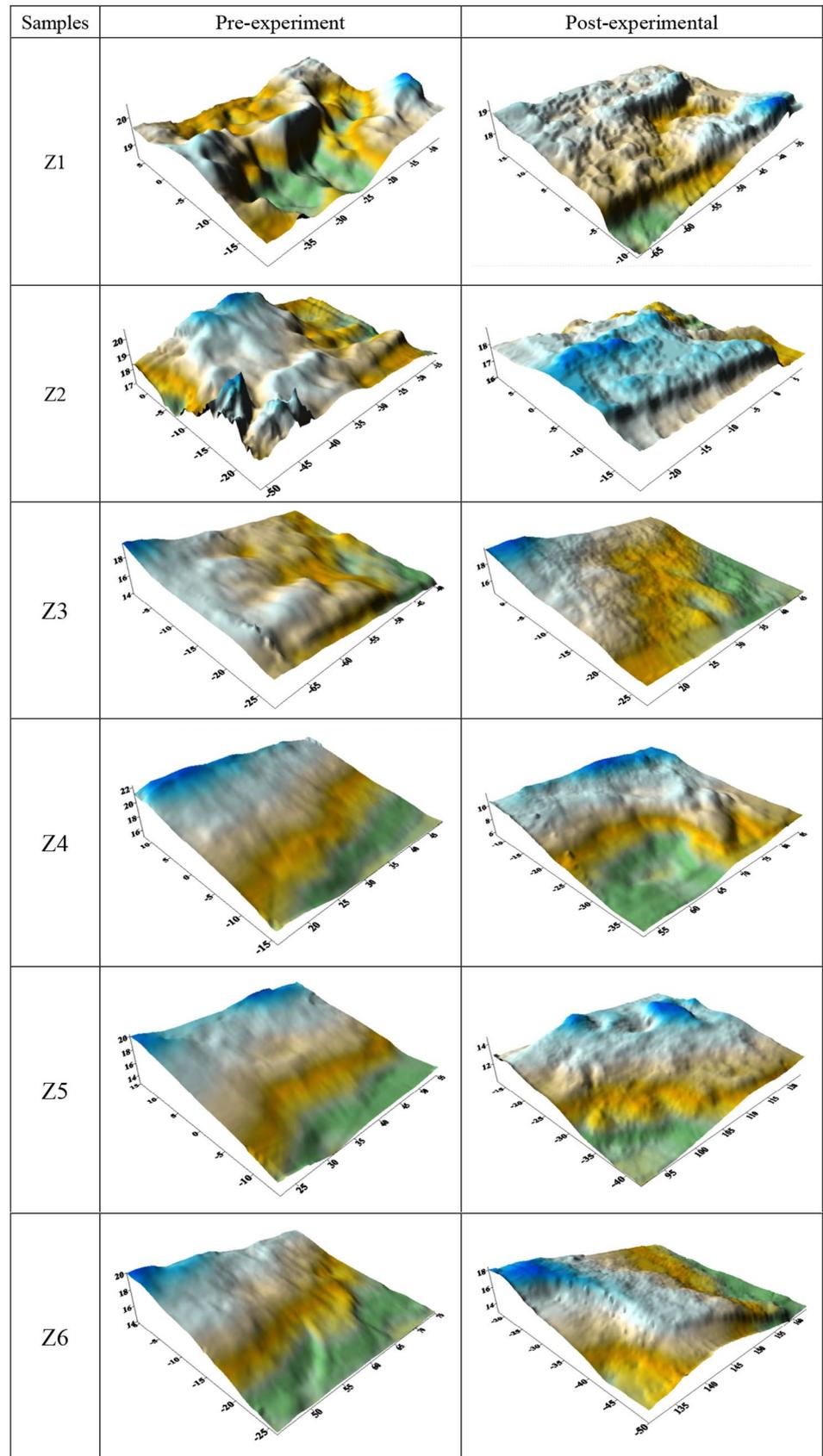
Table 3 The height (z) of weak interlayer in comparison of pre-experiment and post-experiment

	Samples	z_{min} (mm)	z_{max} (mm)	z_{avg} (mm)
Pre-experiment	Z1	18.443	20.487	19.293
	Z2	16.901	20.518	18.870
	Z3	13.928	19.530	16.541
	Z4	15.102	22.295	18.689
	Z5	12.795	20.420	16.890
	Z6	14.006	20.126	16.687
Post-experiment	Z1	17.516	19.433	18.531
	Z2	15.972	18.950	17.896
	Z3	14.487	19.790	16.446
	Z4	5.545	11.932	8.735
	Z5	10.062	14.846	13.068
	Z6	12.899	18.438	15.818

in Ca^{2+}/Mg^{2+} content caught our attention for samples of Z3 and Z6, suggesting that ion exchange hardly occurred in cases of few or no cations.
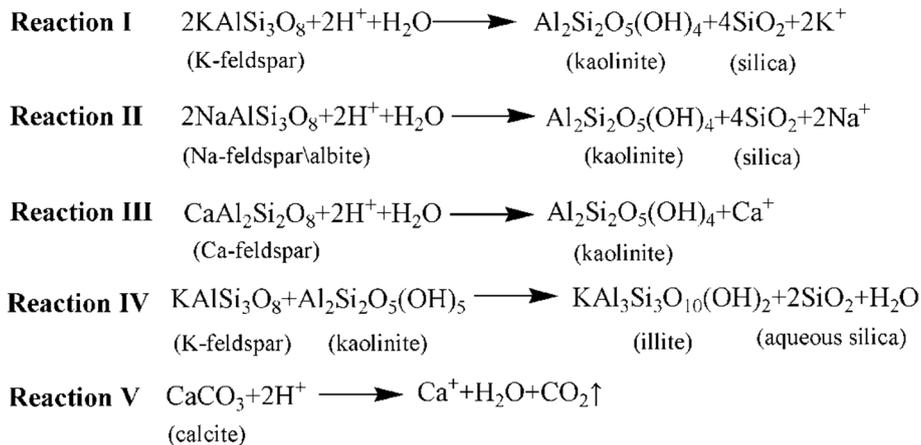
The cations (K^+, Na^+ and Ca^{2+}) that existed in the enclosing structure of AlO_4 tetrahedrons and SiO_4 tetrahedrons in feldspar minerals are closely bound to the O atom around Al and Si atoms, in order to compensate for the net negative charge caused by the presence of Al in the tetrahedral structure. The cations on the surface of feldspar particles were released into the solution through ion exchange with H^+ ions in the acidic solution because of the higher cation exchange capacity of H^+ ions than K^+, Na^+, Ca^{2+} and the reactivity of feldspar in acidic condition, as illustrated in the following reaction I–III, in acidic

solution, the K\Na\Ca-feldspar was altered to produce kaolinite, releasing K^+, Na^+ and Ca^{2+} ions, and further being transformed into illite in reaction IV (Berger et al. 1997; Liu et al. 2018). Based on the XRD results, feldspar mineral in weak interlayer in this experiment was mainly $(Na_{0.98}Ca_{0.02})AlSi_3O_8$, in absence of $KAlSi_3O_8$. Thus, the content of K^+ ions remained essentially unchanged before and after experiment. Otherwise, the decomposition reaction of calcite ($CaCO_3$) took place under the acidic condition, as shown in the following reaction V, followed by the formation of Ca^{2+} ions, resulting in an increase in Ca^{2+} content rather than a decrease.

The physicochemical behavior between water and weak interlayer is a nonlinear dynamic evolution process involving interaction, mutual constraint and mutual feedback. The exchange between H^+ ions and Na^+/Ca^{2+} ions consumed H^+ ions in the acidic solution, and then the pH value of the solution increased. In the alkaline environment with pH > 8.5, the solubility of non-crystalline SiO_2 was rapidly enhanced, forming a negatively charged colloid. The iso-electric point of SiO_2 and Al_2O_3 is pH = 5–6 and pH $\approx$ 8, respectively. From the perspective of iso-electric point and pH value of solution, it was considered that the alkaline groundwater with pH $\approx$ 9 was conductive to the formation of SiO_2 and Al_2O_3 colloids (Wang 1980). The negatively charged SiO_2 colloids and positively charged Al_2O_3 colloids were condensed to form montmorillonite or illite minerals under alkaline and cation-rich condition. Kaolinite easily formed when the water was well-drained, Al-rich and pH value was low (Peng et al. 1991). SiO_2 tends to dissolve in a strong alkaline solution with pH > 10 (Wang 1980).

Table 4 Pre-experimental and post-experimental comparison of ionic concentration in immersion solution

Case		TDS	HCO_3^-	Cl^-	NO_3^-	SO_4^{2-}	K^+	Na^+	Ca^{2+}	Mg^{2+}
pH = 6–7 (Z1Z4)	Pre-	2544	490.17	235.66	0.00	1214.69	3.01	312.33	320.39	143.57
	Post-	3232	22.51	771.06	81.21	2135.89	11.89	724.13	417.14	136.83
	Difference	688	− 467.66	535.40	81.21	921.20	8.88	411.80	96.75	− 6.74
pH = 7–8 (Z2Z5)	Pre-	2544	490.17	235.66	0.00	1214.69	3.01	312.33	320.39	143.57
	Post-	2597	71.58	730.47	78.74	1230.68	7.05	661.88	189.27	102.11
	Difference	35	− 418.59	494.81	78.74	15.99	4.04	349.55	− 131.12	− 41.46
Deionized water (Z3Z6)	Pre-	33	0.50	1.90	0.00	0.00	1.20	0.65	0.07	0.05
	Post-	704	117.50	319.71	38.61	15.20	1.98	227.77	9.28	3.57
	Difference	671	117.00	317.74	38.61	15.20	0.80	227.12	9.21	3.52

Reaction I $2KAlSi_3O_8 + 2H^+ + H_2O \longrightarrow Al_2Si_2O_5(OH)_4 + 4SiO_2 + 2K^+$
(K-feldspar)   (kaolinite)   (silica)

Reaction II $2NaAlSi_3O_8 + 2H^+ + H_2O \longrightarrow Al_2Si_2O_5(OH)_4 + 4SiO_2 + 2Na^+$
(Na-feldspar\albite)   (kaolinite)   (silica)

Reaction III $CaAl_2Si_2O_8 + 2H^+ + H_2O \longrightarrow Al_2Si_2O_5(OH)_4 + Ca^+$
(Ca-feldspar)   (kaolinite)

Reaction IV $KAlSi_3O_8 + Al_2Si_2O_5(OH)_5 \longrightarrow KAl_3Si_3O_{10}(OH)_2 + 2SiO_2 + H_2O$
(K-feldspar)   (kaolinite)   (illite)   (aqueous silica)

Reaction V $CaCO_3 + 2H^+ \longrightarrow Ca^+ + H_2O + CO_2\uparrow$
(calcite)

Mechanism of permeability evolution

A conceptual diagram illustrating the permeability evolution of weak interlayer induced by a physically-chemically mediated erosion in grotto relics was established to deepen and extrapolate the results and observed behaviors in this experiment, as depicted in Fig. 13. Based on the above characterizations before and after the experiment, the changes in mineralogical composition, hydro-chemical data and three-dimensional morphology induced by physically-chemically mediated erosion were highlighted. A coherent explanation of the permeability evolution is that the physically-chemically mediated erosion leads to the formation of fracture channel in weak interlayer under long-term water erosion and hydraulic scouring. At the initial stage, the weak interlayer exhibited a certain thickness sandwiched between intact sandstone layers. When the weak interlayer and intact sandstone were in full contact, the sandwiched structure exhibited a low permeability. In acidic groundwater, the feldspar was easily reacted to produce kaolinite, and the decomposition reaction of calcite occurred. Feldspar and kaolinite can be transformed to montmorillonite or illite minerals under alkaline and cation-rich condition. At the presence of water flow, chemical reactions continuously take place under the changing pH values of groundwater in geological environment, giving rise to the formation of numerous clastic and clay particles in the weak interlayer near the water flow. Under long-term water erosion, more areas in the weak interlayer were transformed into clastic-clay particles filled medium, exhibiting enhanced permeability because

it can be recognized a particle-filled fracture. Finally, particle loss occurred due to hydraulic scouring and fracture channel with a high permeability generated within the weak interlayer.

Permeability quantification

Fig. 13a gives the schematic diagram of a conceptual model containing a weak interlayer at the initial stage. The apparent permeability K_x^* along water flow were expressed as (Ye et al. 2019):

$$K_x^* = \frac{1}{h}\left[\frac{K_1^2 - K_2^2}{\sqrt{\phi_1 K_1} + \sqrt{\phi_2 K_2}} + K_1 b + K_2(h-b)\right], \quad (5)$$

where φ_1 and K_1 are the porosity and permeability of weak interlayer, respectively. As obtained from the above porosity and pore size distribution measurements in Fig. 11, $\varphi_1 = 7.11\%$. According to Kozeny–Carman equation (Assouline and Or 2013; Revil and Cathles 1999; Saxena et al. 2017; Shainberg 1984) in formula (6) and tortuosity (τ) calculation (Yu and Li 2004) in formula (7), K_1 was equal to 2.67×10^{-7} cm/s. φ_2 and K_2 are the porosity and permeability of intact sandstone, $\varphi_2 = 5.73\%$ and $K_2 = 1.53 \times 10^{-8}$ cm/s, which was measured using tri-axial apparatus (MTS815.04), based on steady-state method, as illustrated in Fig. S1.

$$K_1 = \frac{\mu D^2}{72\rho g \tau^2}\frac{\phi_1^3}{(1 - \phi_1^2)} \quad (6)$$
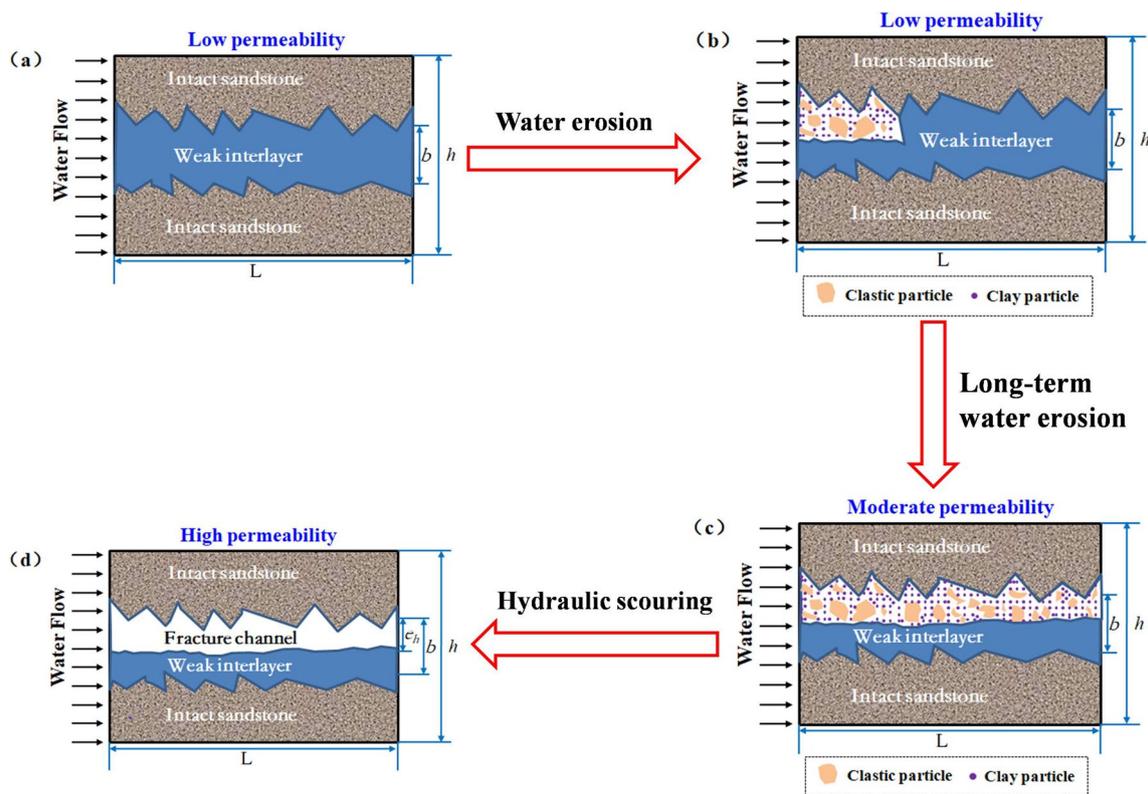
Fig. 13 Conceptual diagram illustrating permeability evolution of weak interlayer induced by physically-chemically mediated erosion in grotto relics: **a** low permeability before water erosion; **b** low permeability after water erosion; **c** moderate permeability after long-term water erosion and **d** high permeability after hydraulic scouring. h and b are the thickness of entire model and weak interlayer, respectively. L is the length of the conceptual model. e_h is the equivalent opening of fracture channel

$$\tau = \frac{1}{2}\left[1 + \frac{1}{2}\sqrt{1-\phi_1} + \sqrt{1-\phi_1}\frac{\sqrt{\left(\frac{1}{\sqrt{1-\phi_1}}-1\right)^2 + \frac{1}{4}}}{1-\sqrt{1-\phi_1}} \right],$$

(7)

where D is grain diameter of the weak interlayer. It was obtained from particle analysis text based on sedimentation method. The average grain diameter of the weak interlayer was 0.011 mm, as displaced in Fig. S2. ρ *is* the density of the fluid, g is the gravity acceleration and μ is the fluid viscosity (Pa s).

The apparent permeability after erosion in Fig. 13d was equivalent to the permeability of fracture channel. For single rough-walled fracture, modified formulas have been proposed to evaluate the equivalent opening e_h based on fracture roughness (Lee 1990; Louis 1972; Su et al. 1994). Based on modified Cubic law, the relationship between the permeability K_f and e_h of a single rough-walled fracture were expressed in formula (8) (Lee 1990).

$$K_x^* \approx K_f = \frac{\rho g e_h^2}{12\mu}$$

(8)

The z_{avg} difference before and after corrosion was considered as the equivalent opening e_h of fracture channel. When the weak interlayer was completely eroded, e_h can be equivalent to the thickness b of the weak interlayer. The permeability of each samples can be calculated according

Table 5 The permeability comparison between pre-experiment and post-experiment

	Samples	e_h (mm)	Pre-experiment	Post-experiment
			K_x^* (cm/s)	K_x^* (cm/s)
pH = 6–7	Z1	0.762	7.78×10^{-8}	4.70×10^{-2}
pH = 7–8	Z2	0.974	9.65×10^{-8}	7.67×10^{-2}
Deionized water	Z3	0.095	1.87×10^{-8}	7.30×10^{-4}
pH = 6–7	Z4	9.954	8.91×10^{-7}	8.01
pH = 7–8	Z5	3.822	3.49×10^{-7}	1.18
Deionized water	Z6	0.869	8.72×10^{-8}	6.11×10^{-2}

to formula (5) and (8), as illustrated in Table 5. The permeability enhanced from of 10^{-7}–10^{-8} cm/s at the initial stage to 8.01–10^{-4} cm/s at the existence of fracture channel.

The pre-experimental flow rate q was given by the following expression:

$$q = \frac{gb^3}{12\mu} \cdot \frac{0.642\phi^3}{(1-\phi)^2} \cdot \frac{\Delta H}{L} = 2.16 \frac{b^3 \Delta H}{L}. \tag{9}$$

The post-experimental flow rate q was exhibited according to the existing equations (Lee 1990):

$$q = \frac{\rho g e_h^3}{12\mu} J = 8077.81 \frac{e_h^3 \Delta H}{L}. \tag{10}$$

Conclusions

The present study aimed to enhance our understanding of physical–chemical erosion on the weak interlayer in grotto relics and its role in permeability evolution. The weak interlayer was characterized by its disintegrability in water, low nano-indentation hardness and modulus strength, as confirmed by morphological features, nano-indentation experiments and Raman spectroscopy analysis. The comparison of pre-experimental and post-experimental XRD results revealed an increase in the total content of clay minerals, indicating a trend towards argillization. In the case of alkalescence groundwater, the weak interlayer encountered ion exchange, absorption and dissolution reactions. Additional decomposition reaction of $CaCO_3$ took place under the acidic groundwater, resulting in an increase in Ca^{2+} content rather than a decrease. The ion exchange process was limited as the groundwater was changed to deionized water. A conceptual diagram illustrating the permeability evolution of weak interlayer induced by physically-chemically mediated erosion in grotto relics was established and a coherent explanation of the permeability evolution is that the physically-chemically mediated erosion leads to the formation of fracture channel in weak interlayer under long-term water erosion and hydraulic scouring. The permeability enhanced from of 10^{-7}–10^{-8} cm/s at the initial stage to 8.01 ~ 10^{-4} cm/s at the existence of fracture channel. As a future study, a long-term experiment will be conducted to clarify the reaction kinetics involving convection, mass transport and chemical reaction.

Author contributions JX Wang participated in the design of the study, carried out all the analyses and drafted the manuscript. The author read and approved the final manuscript.

Declarations

Conflict of interest The authors declare that they have no conflict of interest.

References

Assouline S, Or D (2013) Conceptual and parametric representation of soil hydraulic properties: a review. Vadose Zone J 12(4):vzj2013.2007.0121. https://doi.org/10.2136/vzj2013.07.0121

Berger G, Lacharpagne JC, Velde B, Beaufort D, Lanson B (1997) Kinetic constraints on illitization reactions and the effects of organic diagenesis in sandstone/shale sequences. Appl Geochem 12(1):23–35. https://doi.org/10.1016/S0883-2927(96)00051-0

Blaisonneau A, Peter-Borie M, Gentier S (2016) Evolution of fracture permeability with respect to fluid/rock interactions under thermohydromechanical conditions: development of experimental reactive percolation tests. Geotherm Energy 4(1):3. https://doi.org/10.1186/s40517-016-0045-9

Bourg IC, Ajo-Franklin JB (2017) Clay, water, and salt: controls on the permeability of fine-grained sedimentary rocks. Acc Chem Res 50(9):2067–2074. https://doi.org/10.1021/acs.accounts.7b00261

Chen JY, Huang HW, Zhou ML, Chaiyasarn K (2021) Towards semi-automatic discontinuity characterization in rock tunnel faces using 3D point clouds. Eng Geol 291(2):106232. https://doi.org/10.1016/j.enggeo.2021.106232

Detwiler RL (2008) Experimental observations of deformation caused by mineral dissolution in variable-aperture fractures. J Geophys Res Solid Earth 113(B8):B08202. https://doi.org/10.1029/2008jb005697

Detwiler RL, Rajaram H (2007) Predicting dissolution patterns in variable aperture fractures: evaluation of an enhanced depth-averaged computational model. Water Resour Res 43(4):W04403. https://doi.org/10.1029/2006wr005147

Dong ML, Zhang FM, Hu MJ, Liu C (2020) Study on the influence of anchorage angle on the anchorage effect of soft-hard interbedded toppling deformed rock mass. KSCE J Civ Eng 24(3):2382–2392. https://doi.org/10.1007/s12205-020-2386-y

Gao M, Gao H, Zhao Q, Chang Z, Miao C (2022) Study on stability of anchored slope under static load with weak interlayer. Sustainability 14(17):10542. https://doi.org/10.3390/su141710542

Garcia C S, Nurul Abedin M, Sharma S K, Misra A K, Ismail S, Sandford S P, Elsayed-Ali H (2007) Remote raman sensor system for testing of rocks and minerals. In: Conference on sensors, and command, control, communications, and intelligence (c3i) technologies for homeland security and homeland defense VI

Gu DM, Huang D (2016) A complex rock topple-rock slide failure of an anaclinal rock slope in the Wu Gorge, Yangtze River, China. Eng Geol 208:165–180. https://doi.org/10.1016/j.enggeo.2016.04.037

Hu J, Wen H, Xie Q, Li B, Mo Q (2019) Effects of seepage and weak interlayer on the failure modes of surrounding rock: model tests and numerical analysis. R Soc Open Sci 6(9):190790. https://doi.org/10.1098/rsos.190790

Huang N, Liu R, Jiang Y (2017) Numerical study of the geometrical and hydraulic characteristics of 3D self-affine rough fractures during shear. J Nat Gas Sci Eng 45:127–142. https://doi.org/10.1016/j.jngse.2017.05.018

Jian WX, Yin KL, Ma CQ, Liu LL, Chao Z (2005) Characteristics of incompetent beds in Jurassic red clastic rocks in Wanzhou. Rock Soil Mech 26(6):901–905. https://doi.org/10.16285/j.rsm.2005.06.016

Jin CY, Liu D, Shao AL, Zhao X, Yang L, Fan FQ, Yu KP, Lin RB, Huang JZ, Ding CG (2018) Study on healing technique for weak interlayer and related mechanical properties based on microbially-induced calcium carbonate precipitation. PLoS ONE 13(9):e0203834. https://doi.org/10.1371/journal.pone.0203834

Kalia N, Balakotaiah V (2009) Effect of medium heterogeneities on reactive dissolution of carbonates. Chem Eng Sci 64(2):376–390. https://doi.org/10.1016/j.ces.2008.10.026

Korsakov AV, Zhukov VP, Vandenabeele P (2010) Raman-based geo-barometry of ultrahigh-pressure metamorphic rocks: applications, problems, and perspectives. Anal Bioanal Chem 397(7):2739–2752. https://doi.org/10.1007/s00216-010-3831-4

Lee CH (1990) Flow in fractured rock. University of Arizona, Tucson

Li J, Zhang B, Sui B (2021) Stability analysis of rock slope with multilayer weak interlayer. Adv Civ Eng 2021:1409240. https://doi.org/10.1155/2021/1409240

Liu S, Chen A, Shen Z, Lv Z, Zhang X (2018) Fluid–rock interaction and dissolution of feldspar in the Upper Triassic Xujiahe tight sandstone, western Sichuan Basin, China. Open Geosci 10(1):234–249. https://doi.org/10.1515/geo-2018-0018

Louis C (1972) Rock hydraulics. Springer, Vienna. https://doi.org/10.1007/978-3-7091-4109-0_16

Lu K, Li ZY, Niu RQ, Li F, Pan JW, Li KT, Chen L (2020) Using surface nuclear magnetic resonance and spontaneous potential to investigate the source of water seepage in the JinDeng Temple grottoes, China. J Cult Herit 45:142–151. https://doi.org/10.1016/j.culher.2020.05.006

Luo XY, Cao P, Liu TY, Zhao QX, Meng G, Fan Z, Xie WP (2022) Mechanical behaviour of anchored rock containing weak interlayer under uniaxial compression: laboratory test and coupled DEM–FEM simulation. Minerals 12(4):492. https://doi.org/10.3390/min12040492

McGuire TP, Elsworth D, Karcz Z (2013) Experimental measurements of stress and chemical controls on the evolution of fracture permeability. Transp Porous Media 98(1):15–34. https://doi.org/10.1007/s11242-013-0123-4

Murphy AE, Jakubek RS, Steele A, Fries MD, Glamoclija M (2021) Raman spectroscopy provides insight into carbonate rock fabric based on calcite and dolomite crystal orientation. J Raman Spectrosc 52(6):1155–1166. https://doi.org/10.1002/jrs.6097

Nan SL, Guan WM, Hu T, Shi WS, Zhang JH, Chen H, Cong JY, Liu HB (2021) The influence mechanism of the master weak interlayer on bench blasting effect and its evaluation method. Shock Vib 2021:7814954. https://doi.org/10.1155/2021/7814954

Oliver WC, Pharr GM (1992) An improved technique for determining hardness and elastic modulus using load and displacement sensing indentation. J Mater Res 7:1564–1583. https://doi.org/10.1557/JMR.1992.1564

Oliver WC, Pharr GM (2004) Measurement of hardness and elastic modulus by instrumented indentation: advances in understanding and refinements to methodology. J Mater Res 19(1):3–20. https://doi.org/10.1557/jmr.2004.19.1.3

Peng H, Lv M, Wang J (1991) Hydrogeochemical action in the process of sandwich argillization. J Hohai Univ 19(1):73–78 (**in Chinese**)

Polak A, Elsworth D, Yasuhara H, Grader AS, Halleck PM (2003) Permeability reduction of a natural fracture under net dissolution by hydrothermal fluids. Geophys Res Lett 30(20):2020. https://doi.org/10.1029/2003gl017575

Prinsloo LC, Tournié A, Colomban P, Paris C, Bassett ST (2013) In search of the optimum Raman/IR signatures of potential ingredients used in San/Bushman rock art paint. J Archaeol Sci 40(7):2981–2990. https://doi.org/10.1016/j.jas.2013.02.010

Revil A, Cathles LM (1999) Permeability of shaly sands. Water Resour Res 35(3):651–662. https://doi.org/10.1029/98WR02700

Saxena N, Mavko G, Hofmann R, Srisutthiyakorn N (2017) Estimating permeability from thin sections without reconstruction: digital rock study of 3D properties from 2D images. Comput Geosci 102:79–99. https://doi.org/10.1016/j.cageo.2017.02.014

Shainberg I (1984) Response of soils to sodic and saline conditions. Hilgardia 52(2):1–60. https://doi.org/10.3733/HILG.V52N02P057

Shang J, West LJ, Hencher SR, Zhao Z (2018) Geological discontinuity persistence: Implications and quantification. Eng Geol 241:41–54. https://doi.org/10.1016/j.enggeo.2018.05.010

Shi J, Zhang J, Zhang C, Jiang T, Huang G (2021) Experimental investigation of permeability evolution on sandstone in triaxial and long-term dissolution experiment. Geofluids 2021:5580185. https://doi.org/10.1155/2021/5580185

Sing KSW (1985) Reporting physisorption data for gas/solid systems with special reference to the determination of surface area and porosity. Pure Appl Chem 57(4):603–619. https://doi.org/10.1351/pac198557040603

Su BY, Zhan ML, Zhang ZT (1994) Experimental research of seepage characteristic for filled fracture. Rock Soil Mech 15(4):46–52 (**in Chinese**)

Su MX, Ma XY, Xue YG, Cheng K, Wang P, Liu YM, Yang F (2023) Application of the small fixed-loop transient electromagnetic method in detecting grottoes seepage channel. Environ Earth Sci 82(1):45. https://doi.org/10.1007/s12665-022-10739-5

Sun S, Wang W, Wei J, Song J, Yu Y, He W, Zhang J (2022) Experimental study on microstructure response and mechanical properties of weak interlayer in acidic environment. Nat Hazards 112(1):327–348. https://doi.org/10.1007/s11069-021-05183-w

Sun B, Ma FY, Zhang H, Peng NB, Zhang P (2023) Carbon quantum dots as a tracer of water seepage sources and pathways in grottoes. Herit Sci 11(1):211. https://doi.org/10.1186/s40494-023-01058-4

Tse R (1979) Estimating joint roughness coefficients. Int J Rock Mech Min Sci 16(5):303–307. https://doi.org/10.1016/0148-9062(79)90241-9

Wang YL (1980) Physicochemical investigation of genesis and properties of argilled interlayer in Gezhouba, China. Hydrol Eng Geol 04:5–11. https://doi.org/10.16030/j.cnki.issn.1000-3665

Wang JX (2023) Visualizing water seepage dynamics in grotto relics via atom-based representative model. Herit Sci 11(1):5. https://doi.org/10.1186/s40494-022-00832-0

Wei E, Hu B, Tian K, Cen P, Zhang Z, Wang Z, Chang S, Cui X (2022) Study on the nonlinear damage creep model of the weak interlayer. Adv Civ Eng 2022:1–8. https://doi.org/10.1155/2022/3566521

Yasuhara H, Polak A, Mitani Y, Grader A, Halleck P, Elsworth D (2006) Evolution of fracture permeability through fluid–rock reaction under hydrothermal conditions. Earth Planet Sci Lett 244(1–2):186–200. https://doi.org/10.1016/j.epsl.2006.01.046

Ye HX, Dong M, Dong HZ (2011) Mechanism research on concentrated leakage passage formed by water flow erosion in weak structure plane. J Disaster Prev Mitig Eng 31(2):173–179. https://doi.org/10.1007/s12517-021-09271-w

Ye F, Duan JC, Fu WX, Yuan XY (2019) Permeability properties of jointed rock with periodic partially filled fractures. Geofluids 2019:1–14. https://doi.org/10.1155/2019/4039024

Yu BM, Li JH (2004) A geometry model for tortuosity of flow path in porous media. Chin Phys Lett 21:1569–1571. https://doi.org/10.1088/0256-307X/21/8/044

Zhang JS, Yang H, Ye X, Wang SL (2023) Water-rock(soil) chemical reaction during formation process of weak interlayers in red bedded accumulation. Yangtze River 54(12):142–146 (**in Chinese**)

Zhou Z, Zhang J, Cai X, Wang S, Du X, Zang H (2020) Permeability experiment of fractured rock with rough surfaces under different stress conditions. Geofluids 2020:1–15. https://doi.org/10.1155/2020/9030484

Zhu CL, Lei XZ, Fu WX, Ye F (2019) Research on water depth of weak interlayer containing continuous cracks suffering from hydraulic erosion. China Rural Water Hydropower 2:139–154 (**in Chinese**)

Zhu CL, Lei XZ, Ye F, Fu WX (2020a) Contact scouring mechanism of seepage in weak interlayers. China Rural Water Hydropower 1:176–180 (**in Chinese**)

Zhu X, Liu G, Gao F, Ye D, Luo J, Liu R (2020b) A complex network model for analysis of fractured rock permeability. Adv Civ Eng 2020:1–10. https://doi.org/10.1155/2020/8824082